Chemical Engineering Journal 238 (2014) 66–77

Contents lists available at ScienceDirect

Chemical Engineering Journal

journal homepage: www.elsevier.com/locate/cej

Flow field simulation and mixing efficiency assessment of the multi-inlet vortex mixer for molybdenum sulfide nanoparticle precipitation

S. Bensaid *, F.A. Deorsola, D.L. Marchisio, N. Russo, D. Fino

Department of Applied Science and Technology, Politecnico di Torino, Corso Duca degli Abruzzi 24, 10129 Torino, Italy

HIGHLIGHTS

- MoS_2 nano-lubricants with primary particle sizes from 60 to 135 nm were obtained.
- MoS_2 nanoparticle synthesis was performed in a multi-inlet vortex micro-mixer.
- The mixer flow field was computed at a *Re* of the mixing chamber of 832, 4160 and 8320.
- The reactants were fully macro-mixed (mixture fraction = 0.5) already at *Re* = 4160.
- The micro-scale variance of the mixture fraction was 0.03 at *Re* = 4160 and 0.008 at *Re* = 8320.

ARTICLE INFO

Article history:
Available online 25 September 2013

Keywords:
Lubricants
Molybdenum disulfide
Nanoparticle
Precipitation
Micro-mixer
CFD modeling

ABSTRACT

Molybdenum sulfide nanoparticles (NP) have been successfully obtained, for lubricant applications, by means of a wet chemical synthesis in an aqueous solution employing ammonium molybdate, citric acid and ammonium sulfide as the reactants. The production of MoS_2 NP has been performed in a multi-inlet vortex mixer, which has the ability to ensure fast mixing, induced by a confined turbulent flow inside the precipitation chamber, to suitably control the NP size distribution.

In particular, three inlet flow rates, corresponding to Reynolds numbers in the mixing chamber (hereafter named Re_c) of 832, 4160 and 8320 were employed, which resulted in NP primary particle average sizes of 135 nm, 84 nm and 60 nm, respectively.

The flow field of the multi-inlet vortex mixer was therefore investigated through computational fluid dynamic simulations, in order to assess the mixing efficiency of this device, with respect to the different operating conditions leading to these size differences in the MoS_2 product.

Both laminar and turbulent (LES and RANS k–ε) models were employed to simulate the profiles of tangential and radial velocity inside the micro-mixer. From the comparison with μPIV measurements, it was found that the laminar model was the most suitable one for the case at a Re_c equal to 832, while turbulence had to be taken into account for higher Reynolds numbers (namely 4160 and 8320).

The degree of mixing was assessed through the mean mixture fraction approach by resorting to a micro-mixing model. The degree of segregation of the reactants was assessed at the macro-scale, as well as at the micro-scale (i.e. the molecular level). It emerged that the only satisfactory condition in terms of micro-mixing was the one at a Re_c of 8320, which ensured that an effective mixing of the reactants down to the molecular scale was reached within the mixing chamber.

The operating conditions ensuring optimal mixing were assessed, and the experimental results were discussed based on these evaluations.

1. Introduction

Advanced lubricant nanomaterials are nowadays of great interest for their potential in reducing friction and enhancing protection against wear, when incorporated in full lubricant formulations in a stable way [1]: as a matter of fact, they can contribute to substantial energy savings, as well as to reduce equipment maintenance and lengthen the life of the machines.

Transition metal dichalcogenides with the generic formula MX_2 (M = W, Mo; X = S, Se) seem to be very promising materials to be dispersed as nanoparticles in the engine oil matrix [2].

Several nanoparticle synthesis techniques and morphologies have been investigated: a pioneering work in this field has been carried out by Tenne and co-workers, who first synthesized these materials through the reaction between MO_3 and H_2S in a fluidized

* Corresponding author. Tel.: +39 011 0904662; fax: +39 011 0904699.
E-mail address: samir.bensaid@polito.it (S. Bensaid).

1385-8947/$ - see front matter © 2013 Elsevier B.V. All rights reserved.
http://dx.doi.org/10.1016/j.cej.2013.09.065

Nomenclature

List of symbols

C_φ	mechanical-to-scalar timescale ratio
C_μ	constant for turbulent diffusivity calculation
D	hydraulic diameter of the inlet channel
D_c	diameter of the mixing chamber
f_ξ	probability density function (PDF)
k	turbulent kinetic energy
K	number of inlet channels in the MIVM
N	number of environments
p_n	volume fraction of the environment
Re_c	Reynolds number in the mixing chamber
Re_j	Reynolds number in the inlet channel
Re_l	local turbulent Reynolds number
Sc_t	turbulent Schmidt number
$\langle u_i \rangle$	Reynolds-averaged velocity
V	mean velocity in the inlet channel
x	position vector in the computational domain

Greek letters

ε	turbulent dissipation rate
λ_M	micro-mixing rate
Γ_t	turbulent diffusivity
ξ_n	local mixture fraction
ξ_n	mixture fraction
$\langle \xi \rangle$	mean mixture fraction
$\langle \xi'^2 \rangle_{LS}$	large scale variance
$\langle \xi'^2 \rangle_{SS}$	small scale variance
ν	kinematic viscosity

Subscripts

n,1,2	Environments (n: generic, 1 or 2: specific)

Abbreviations

CIJR	Confined Impinging Jets Reactor
CFD	Computational Fluid Dynamics
DLS	dynamic light scattering
LES	Large Eddy Simulation
LS	Large Scale
MIVM	multi-inlet vortex mixer
MIVR	multi-inlet vortex reactor
NP	nanoparticle
PDF	probability density function
PSD	particle size distribution
RANS	Reynolds-Averaged Navier–Stokes
SS	Small Scale
μPIV	micro-Particle Image Velocimetry

bed, in a reducing atmosphere at high temperature, to obtain the corresponding sulfide (WS_2 or MoS_2) [3]. The lubrication mechanisms of these metal sulfides, often called inorganic fullerenes due to their peculiar structure of spherical concentric layers, is currently debated; however, several studies indicate that an exfoliation process of these layers, and the consequent liberation of nanosheets directly inside the surface contact area, is the prevalent lubricating mechanism for these systems [4,5].

Other techniques can be used for the sulfidization of MO_3 into WS_2 or MoS_2, such as spray drying [6], or chemical vapor condensation [7]; however all these methods are characterized by high temperatures (800–1000 °C) in the presence of H_2 or H_2S, which involves a certain complexity of the equipment. Milder conditions can be used for liquid phase synthesis of the sulfides, either in aqueous [8] or organic solution [9].

One major requirement for the application of these nanoparticles as lubricant oil additives, in substitution to the currently adopted ones, is their constraint not to produce any related harmful emission, which could modify the nominal performances of the catalytic substrates present in the after-treatment line, through sulfur-related catalyst aging or excessive ash formation [10,11], and possibly affect their lifetime durability.

The present study focuses on the synthesis of MoS_2 nanoparticles which have to be incorporated in engine lubricant oils, and specifically on the micro-fluidic device to achieve this synthesis. A technique has been devised [12], which is based on the preparation of an aqueous solution of citric acid and ammonium molybdate to form a complex of molybdenum(IV), to which a suitable amount of ammonium sulfide was added to obtain MoS_2. It is worth mentioning that the chemistry of molybdenum and molybdenum compounds is quite complex and it is very difficult to provide exact and reliable reactions [13]. The ammonium molybdate is supposed to decompose, in an acid environment, into molybdenum trioxide and its hydrated forms, also referred to molybdic acid. The citric acid can react with both molybdic acid and molybdenum trioxide. In the first case, some various Mo-citrate complexes are formed, the composition of which is not defined and for this reason it is difficult to draw up univocal chemical reactions. In the second case, the citric acid reduces the Mo (VI) to a lower (IV) valence state, in the form of molybdenum dioxide. This compound reacts with the ammonium sulfide with the final formation of molybdenum disulfide.

This synthesis resorts to a simple and scalable process, and involves low-cost reagents, instead of other above-mentioned complex reaction methods. This synthesis route is extremely versatile since it can be adapted for continuous MoS_2 particle production, in specific devices that allow to control the particle diameter and obtain reproducible results in terms of particle size distribution [12].

MoS_2 precipitation is a fast process and thus the rate and extension of mixing is determining for the process outcome: because of their ability to achieve the high mixing efficiencies necessary in the precipitation process, passive micro-mixers are here investigated for this application. The term micro-fluidic device strictly refers to systems with characteristic length-scales that are in the range of micrometers. Small dimensions lead to behaviors strictly controlled by molecular phenomena [14], allowing rapid diffusive mixing with time-scales ranging from tens to hundreds of milliseconds. Very interesting is also the recent investigation of large micro-mixers (with characteristics length-scales ranging from hundreds of micrometers to a few millimeters) in which some flow instability is allowed to develop resulting, under particular operating conditions, in turbulent flow and turbulent mixing [15]. These devices present the main advantages of passive micro-mixers, such as more controlled process conditions, better and faster homogenization of the feed streams, short mean residence time and narrow residence time distribution, combined with other additional advantages, such as limited power consumption (when compared with traditional micro-fluidic systems) and ease of scalability for process intensification.

Examples of these kind of mixer configuration are the T-Mixer [16], the multi-inlet vortex mixer (MIVM) [17] and the Confined

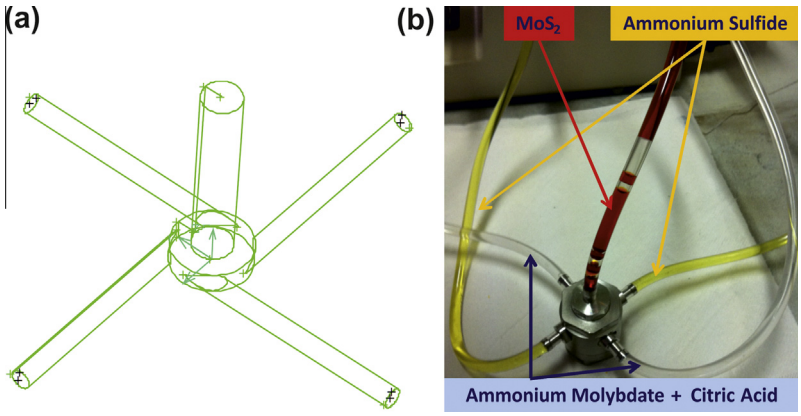

Fig. 1. (a) Geometry of the MIVM employed for and (b) MoS_2 nanoparticle synthesis.

Impinging Jets Reactor (CIJR) [18]: these three categories of mixers differ by the size of the mixing chamber, the number of inlets, the position of the inlets (axially aligned or unaligned) and the size of the outlet channels with respect to the inlet ones. Various geometries and dimensions were studied experimentally by Johnson and Prud'homme [18] and their mixing efficiency was evaluated by means of a parallel competitive reactions scheme. Following that work, Liu and Fox [19] applied Computational Fluid Dynamics (CFD) in order to develop a model able to predict the extent of mixing in the CIJR and found good agreement with the experimental data. They employed the Reynolds-Averaged Navier–Stokes equations (RANS) to model the inter flow field of the micro-mixer. The outcome of the latter investigation showed that the choice of the turbulence model and the near wall treatment has a great effect on the final model predictions, and therefore an independent validation of flow and turbulent field is needed. Other works employed Large Eddy Simulation (LES) to reach a more accurate prediction of the internal flow-field of micro-mixer [20]. In both studies, modeling results were validated against micro-Particle Image Velocimetry (μPIV).

In our research activity, the use of the Vortex-shaped micro-mixer, called multi-inlet vortex mixer (MIVM) or multi-inlet vortex reactor (MIVR), has successfully been employed to synthesize MoS_2 nanoparticles, in continuous mode, and with the possibility to tune the particle sizes according to the fluid-dynamics inside the reactor [12]. In this work, an insight on the flow-field of the MIVM being used for the experimental activity is attempted: computational fluid dynamic simulations were used to provide detailed predictions of spatial distributions of reactant concentrations, through which the effectiveness of the achieved mixing can be assessed at the different operating conditions selected for the experimental investigations.

The flow-field of the MIVM was simulated with a laminar model and a turbulent one based on the Reynolds Average Navier–Stokes equations (RANS) approach, depending on the operating conditions and the resulting flow regime. Among the different options, the k–ε turbulent model was mainly used in this work. The proper selection of either laminar or turbulent models with respect to the inlet conditions was validated against experimental measurements based on μPIV available from [20], dealing with a very similar geometry of the MIVM, later detailed in this work.

The ability of this MIVM to bring the two separate reactants, namely the solution containing the molybdenum(IV) complex with citric acid and the one of ammonium sulfide, into close (i.e. molecular) contact to obtain MoS_2, was computed through a molecular mixing model called DQMOM–IEM: this approach describes mixing in terms of the mixture fraction probability density function approach by using the Direct Quadrature Method Of Moments (DQMOM) coupled with the Interaction and Exchange with the Mean (IEM) [21–22].

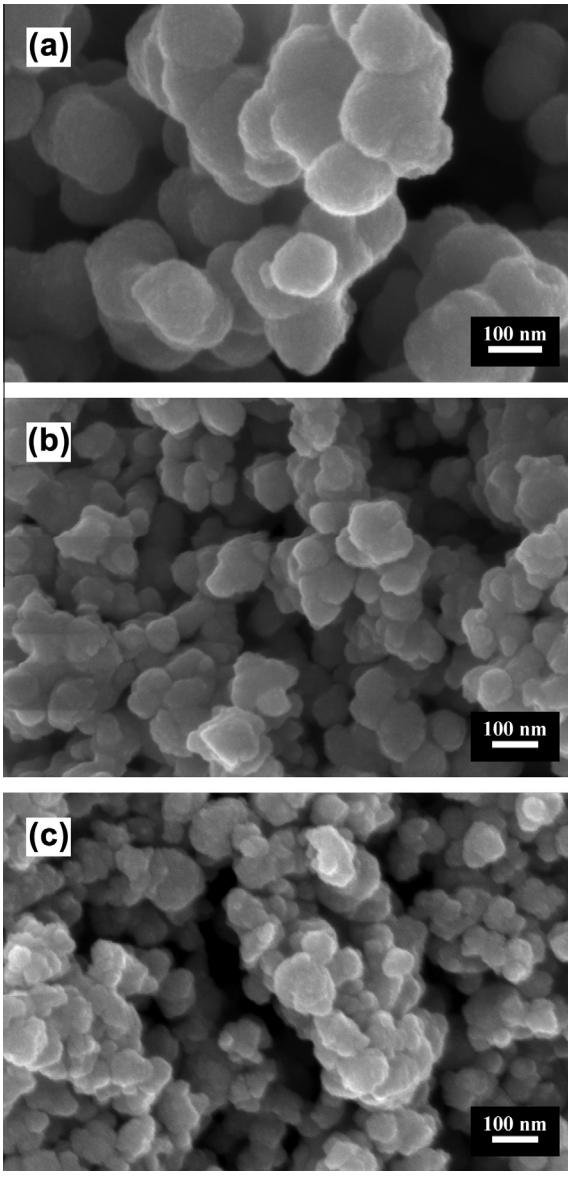

Fig. 2. FESEM micrographs of the MoS_2 nanoparticles obtained with different inlet flow rates: (a) 2 ml/min, (b) 10 ml/min and (c) 20 ml/min.

Table 1
Average diameter of the MoS_2 primary particles, calculated by FESEM micrographs.

Flow rate (ml/min)	Average diameter of primary particle (nm)
2	135 ± 42
10	84 ± 17
20	60 ± 11

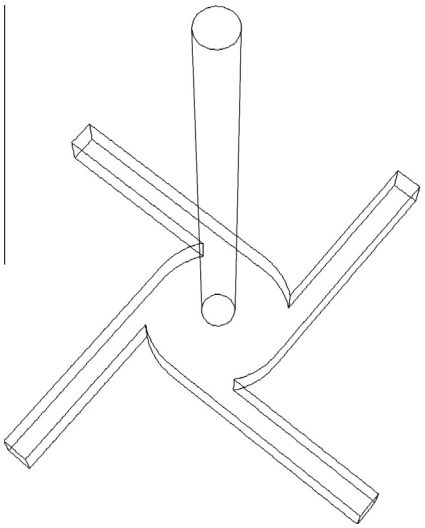

Fig. 3. Detail of the computational volume of the reference MIVM used for CFD validation, based on the geometry described in [20].

The present article is organized as follows: in Section 2, the turbulence and micro-mixing models employed in this work are detailed; then, in Section 3, the geometry of the mixer, the investigated operating conditions, and the numerical details of the performed simulations are given; lastly, the simulation results are presented and discussed with respect the experimental findings described in [12] and here recalled.

2. Modeling approach

For the three-dimensional simulations of the MIVM flow-field, the most suitable model to describe the internal flow field inside the mixer, at the given operating conditions, was selected based on the experimental velocity profiles from μPIV available in [20]. The experimental data were very close to the Reynolds of our work, and the results of the performed simulations could therefore be extended to our system. The system in [20] was simulated under laminar conditions for low Reynolds number cases, while both the standard k–ε RANS and Large Eddy Simulation (LES) models were instead employed for the simulations performed at higher Reynolds numbers. The full set of simulation results are later presented and discussed in this work, but it can be anticipated that the RANS model was quite satisfactory in predicting the internal flow field of the MIVM, and was therefore selected as the most suitable turbulent model for this study. Hence, although LES allows a more accurate prediction of the internal flow-field of this micro-mixer, the implementation of the micro-mixing model was limited to RANS, because it is computationally much cheaper.

DQMOM–IEM model resolves the system micro-mixing dynamics through the use of a functional form for the presumed probability density function (PDF) f_ξ of the mixture fraction ξ. The mixture fraction is a non-reacting scalar that lies between zero and one and quantifies, in our case, the amount of fluid coming from the MIVM inlets containing the solution of molybdenum(IV) complex with citric acid with respect to the ones containing ammonium sulfide. In particular, a quadrature formula is used for describing the mixture fraction PDF, each node representing a fluid environment with a specific value of volume fraction or weight, p_n, and local mixture fraction, ξ_n for a total number of nodes or environments equal to N, a corresponding the following functional form:

$$f_\xi(\mathbf{x};\xi) = \sum_{n=1}^{N} p_n(\mathbf{x})\delta(\xi - \xi_n(\mathbf{x})), \tag{1}$$

in which ($\mathbf{x}$) is the position vector. The solution of the full set of transport equations for $p_n(\mathbf{x})$ and $p_n\xi_n(\mathbf{x})$, allows to completely characterize the mixing dynamics at all scales [21–23]. In particular, the transport equation relative to the probability of the first environment $p_1(\mathbf{x})$ is written as follows:

$$\frac{\partial p_1}{\partial t} + \langle u_i\rangle \frac{\partial p_1}{\partial x_i} - \frac{\partial}{\partial x_i}\left(\Gamma_t \frac{\partial p_1}{\partial x_i}\right) = 0; \tag{2}$$

where $\langle u_i\rangle$ is the Reynolds-averaged velocity and Γ_t is the turbulent diffusivity, the latter being defined as:

$$\Gamma_t = \frac{C_\mu}{Sc_t}\frac{k^2}{\varepsilon}, \tag{3}$$

with C_μ = 0.09, and calculated through a turbulent Schmidt number, Sc_t, equal to 0.7 [24]; k and ε denote the turbulent kinetic energy and turbulent dissipation rate, respectively, and are computed using the k–ε model.

In the $p_1(\mathbf{x})$ balance expression the density does not explicitly appear since it is considered to be constant, as only aqueous solutions with equal and constant density are considered in this work. If N = 2, then $p_2(\mathbf{x})$ is simply $1-p_1(\mathbf{x})$ by definition, because the sum of all environment volume fractions is equal to the unity.

The second and third transport equations to be solved are relative to the weighted mixture fraction in the first and second environment:

$$\frac{\partial p_1\xi_1}{\partial t} + \langle u_i\rangle \frac{\partial p_1\xi_1}{\partial x_i} - \frac{\partial}{\partial x_i}\left(\Gamma_t \frac{\partial p_1\xi_1}{\partial x_i}\right) = \gamma_M p_1 p_2(\xi_2 - \xi_1) + \frac{\Gamma_t}{\xi_1 - \xi_2}\left(p_1\frac{\partial \xi_1}{\partial x_i}\frac{\partial \xi_1}{\partial x_i} + p_2\frac{\partial \xi_2}{\partial x_i}\frac{\partial \xi_2}{\partial x_i}\right); \tag{4}$$

$$\frac{\partial p_2\xi_2}{\partial t} + \langle u_i\rangle \frac{\partial p_2\xi_2}{\partial x_i} - \frac{\partial}{\partial x_i}\left(\Gamma_t \frac{\partial p_2\xi_2}{\partial x_i}\right) = \gamma_M p_1 p_2(\xi_1 - \xi_2) + \frac{\Gamma_t}{\xi_2 - \xi_1}\left(p_1\frac{\partial \xi_1}{\partial x_i}\frac{\partial \xi_1}{\partial x_i} + p_2\frac{\partial \xi_2}{\partial x_i}\frac{\partial \xi_2}{\partial x_i}\right). \tag{5}$$

The first term on the right hand side is the micro-mixing term according to the IEM model, in which the micro-mixing rate γ_M appears, and the last term is the correction term, that originates from the finite mode representation, and ensures that scalar variance is correctly predicted. The expression of the micro-mixing rate is:

$$\gamma_M = \frac{C_\varphi}{2}\frac{\varepsilon}{k}. \tag{6}$$

The nominal value of the mechanical-to-scalar timescale ratio C_φ is a function of local turbulent Reynolds number Re_l, defined as:

$$Re_l = \frac{k}{(s\nu)^{1/2}}, \tag{7}$$

and has a polynomial expression reported in [24].

As a result, the two terms in right hand sides of the $p_1\xi_1$ and $p_2\xi_2$ balance equations represent micro-mixing; if these terms are negligible, i.e. the variation of ξ_1 and ξ_2 is the mixing chamber is limited, then no mixing occurs on the molecular level and thus no reactions take place.

From the computed values of p_n and ξ_n, the mean mixture fraction $\langle\xi\rangle$ can be calculated; for N = 2, it is calculated in the following expression:

$$\langle\xi\rangle(\mathbf{x}) = \int_0^1 f_{\tilde{\xi}}(\mathbf{x};\xi)d\xi = p_1(\mathbf{x})\xi_1(\mathbf{x}) + p_2(\mathbf{x})\xi_2(\mathbf{x}). \quad (8)$$

The difference between $\langle\xi\rangle$ and its value corresponding to complete mixing, $\bar{\xi}$, can be calculated in each computational cell is called the Large Scale (LS) Variance:

$$\langle\xi'^2\rangle_{LS}(\mathbf{x}) = (\langle\xi\rangle(\mathbf{x}) - \bar{\xi})^2, \quad (9)$$

and represents the level of mixing at the macro-scale. On the other hand, the Small Scale (SS) Variance, $\langle\xi'^2\rangle_{SS}$, contains information concerning the level of segregation at the micro- (or molecular) scale, and is calculated as:

$$\langle\xi'^2\rangle_{SS}(\mathbf{x}) = \int_0^1 (\xi - \langle\xi\rangle)^2 f_{\tilde{\xi}}(\mathbf{x};\xi)d\xi = p_1(\mathbf{x})p_2(\mathbf{x})(\xi_1(\mathbf{x}) - \xi_2(\mathbf{x}))^2. \quad (10)$$

3. Operating conditions and numerical details

3.1. Experimental method

The geometry of the investigated MIVM for MoS_2 production (Fig. 1a) is characterized by four tangential circular inlets, each one with an internal diameter of 1 mm, and a reaction chamber of 4 mm in diameter and 1 mm in height. The channels and the chamber have the same height and no cross flow area reduction is induced in the flow which enters the chamber. The product is discharged in a 2 mm diameter duct, perpendicular to inlet radial flows. The four inlets were connected by means of polypropylene pipes to four 20 ml syringes, and driven by a KD Scientific KDS220 infusion syringe pump. The syringes were filled in pairs with the two reactant solutions: a solution of molybdate tetrahydrate and citric acid (1:3 Mo:citrate molar ratio) at 27%wt in water, and solution of ammonium sulfide at 20%wt in water. The solutions were fed to the four channels (Fig. 1b) alternating the molybdate tetrahydrate and citric acid solution with the ammonium sulfide solution, to maximize the mixing efficiency.

The described MIVM was employed for the synthesis of MoS_2 nanoparticles. The particle size distribution (PSD) of the produced nanoparticle aggregates was measured by dynamic light scattering (DLS) with Malvern Nano ZS90 [12], but not directly used in this modeling activity because it allows to estimate the aggregate PSD size only. The micro-structural characterization was performed through a field emission scanning electron microscopy (Leo Supra 40) equipped with an EDS probe, which allowed to estimate the mean diameter of the primary particles [12] (Fig. 2): it

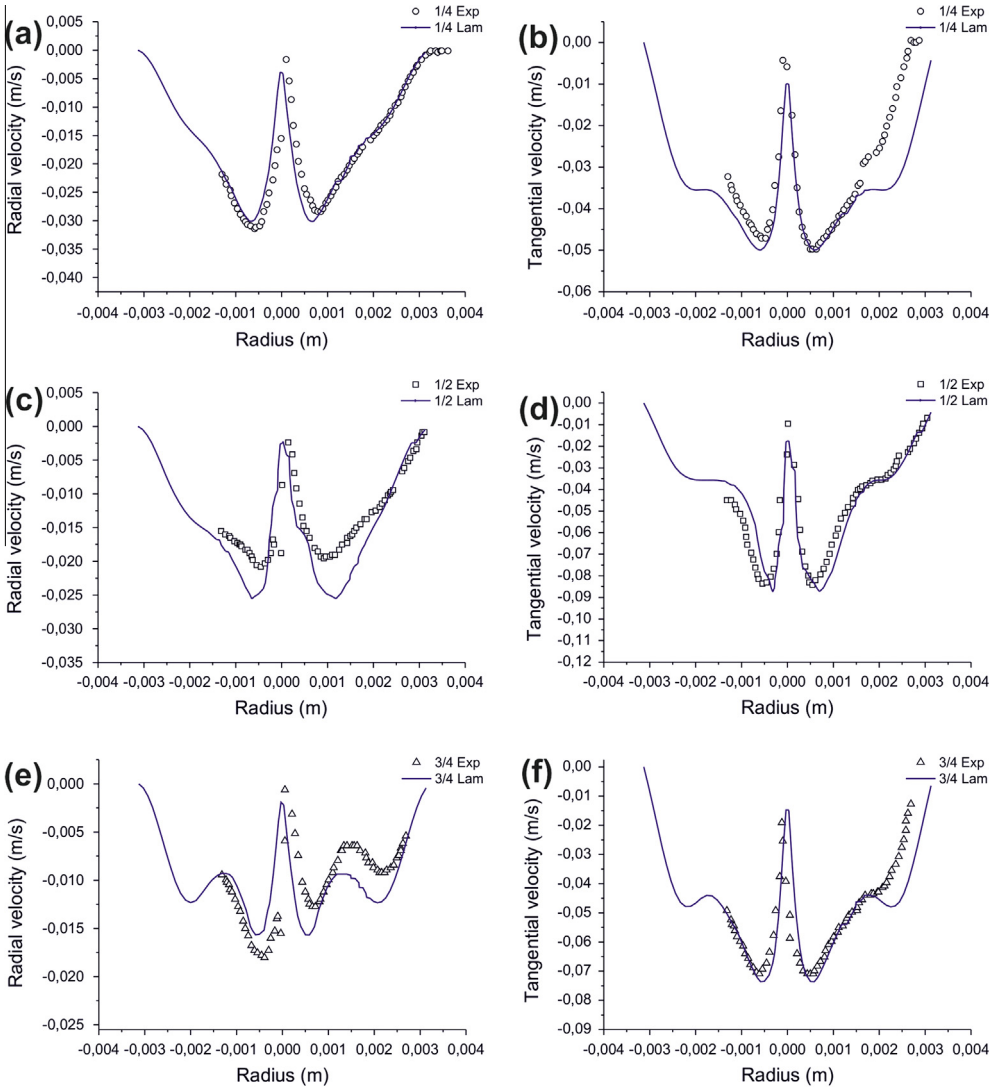

Fig. 4. Radial and tangential velocity profiles of the reference MIVM in Fig. 3, computed on a radial segment lying on horizontal planes at 1/4, 1/2 and 3/4 of the mixing chamber height, for Re_j of 53 (dots: experimental μPIV values; blue solid line: simulation with laminar model). (For interpretation of the references to colour in this figure legend, the reader is referred to the web version of this article.)

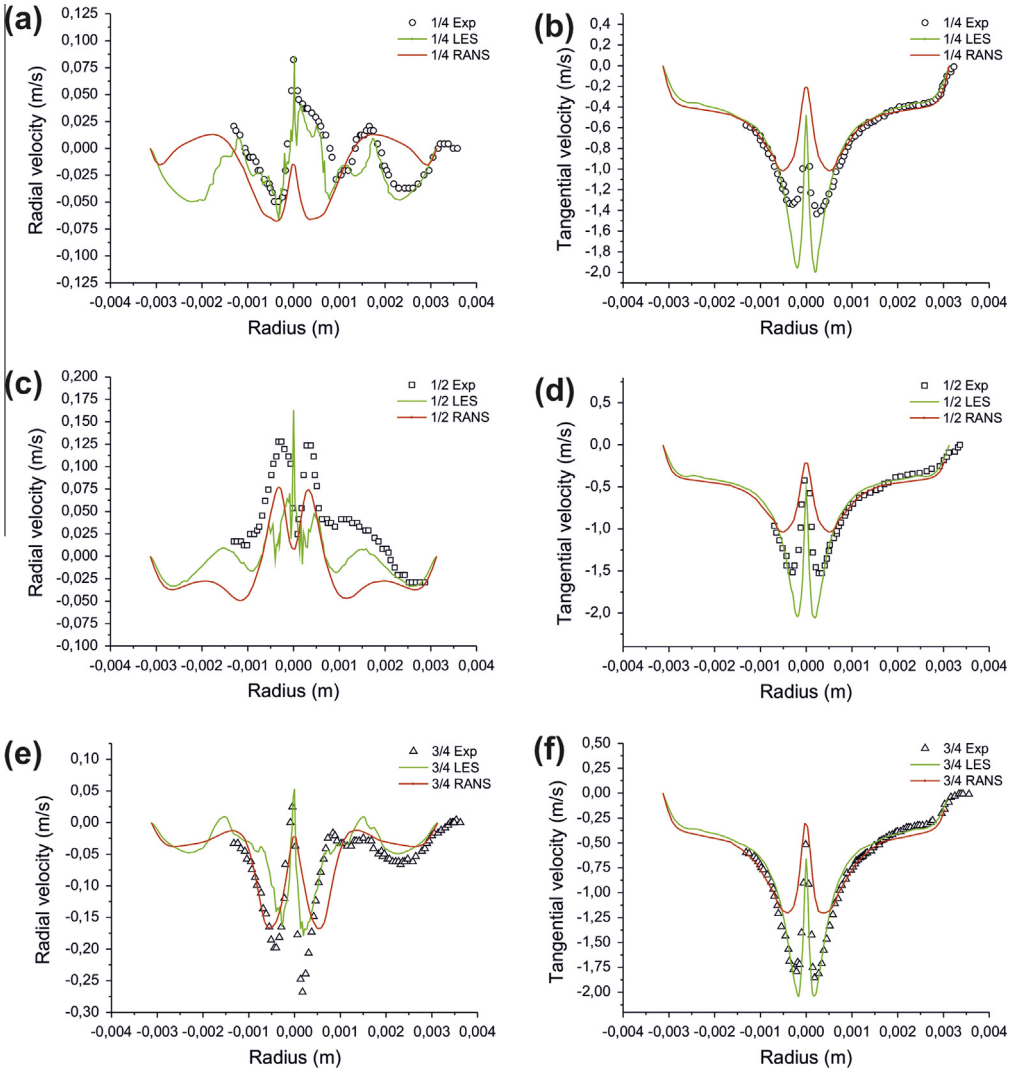

Fig. 5. Radial and tangential velocity profiles of the reference MIVM in Fig. 3, computed on a radial segment lying on horizontal planes at 1/4, 1/2 and 3/4 of the mixing chamber height, for Re_j of 240 (dots: experimental μPIV values; green solid line: simulation with LES model; red solid line: simulation with RANS standard k–ε model). (For interpretation of the references to colour in this figure legend, the reader is referred to the web version of this article.)

was found that the dimension of the primary particles was considerably reduced by increasing the inlet flow rate, which could be tuned to obtained the desired nanoparticle sizes. The data of the primary particle diameters (gathered in Table 1) obtained in [12] were taken as a measure of the overall mixing efficiency in the MIVM. In fact, faster mixing leads to higher values of super-saturation, which in turn increases the nucleation rate of the primary particles. High nucleation rates increase the number of primary particles being formed, and consume at a greater extent the MoS_2 precursors subsequently involved in particle growth phenomena, thus generally leading to smaller primary particles than in cases characterized by low super-saturation degrees [25]. Therefore, smaller primary particles indicate a higher degree of mixing at all scales (including the molecular level which is the most difficult to achieve especially in liquid systems). To this end, the mixing in the MIVM was simulated with the aim of demonstrating that the control of the MoS_2 primary particle size, through the manipulation of the inlet flow rates, was due to the discriminating effect of the achieved mixing degree. It is worth mentioning that the turbulence of the system could either increase the size of the primary particle aggregates by enhancing the collision frequency, or keep the overall dimension of the aggregate low if the shear stresses exerted by the fluid on the aggregate exceed the inter-particle forces. However, these latter aspects were not modeled here, since only macro- and micro-mixing phenomena were investigated in this work.

3.2. Numerical simulations

Initially, the μPIV experimental data described in [20] were modeled through CFD to check the suitability of the laminar and turbulent (k–ε RANS and LES) models to describe the system. The geometry of the micro-mixer in [20], which is depicted in Fig. 3, is characterized by a rectangular shape of the four inlet channels (height:1.53 mm, width:1.19 mm), a cylindrical mixing chamber of 6.26 mm in diameter, and an outlet channel diameter of 1.4 mm. It is worth mentioning that the circular geometry of the inlet channels of the MIVM for MoS_2 synthesis allows an easier cleaning maintenance of the micro-device, while the inlet channels' rectangular shape designed in [20] was functional to μPIV experimental data acquisition. The operating conditions, at which the micro-mixer in [20] was simulated, were at a "jet" Reynolds numbers in the inlet channels of 53 and 240. The definition of a "jet" Reynolds number is:

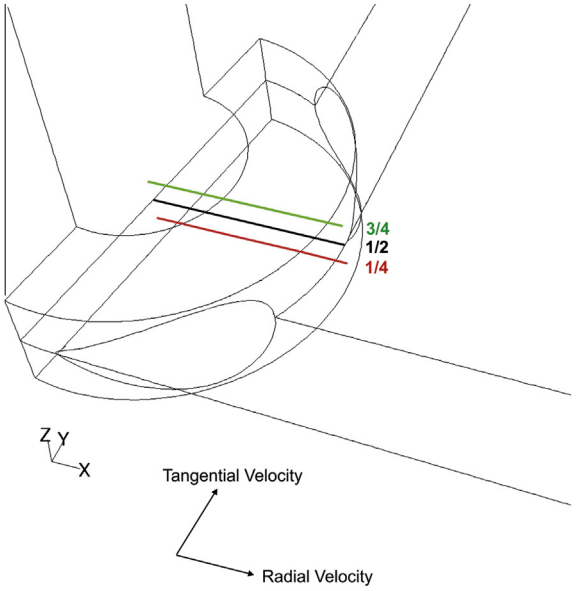

Fig. 6. Detail of the computational volume of the MIVM for MoS_2 synthesis, and of the three radial segments, lying on horizontal planes at 1/4, 1/2 and 3/4 of the reacting chamber height.

$$Re_j = \frac{\rho D V}{\mu} \tag{11}$$

where D is the hydraulic diameter of the channel and V is the mean velocity in each channel.

Conversely, in the mixing chamber, the Reynolds number can be calculated as [26]:

$$Re_c = \sum_{i=1}^{k} \frac{\rho D_c V_i}{\mu} \tag{12}$$

where D_c is the chamber diameter, V_i is the mean velocity in each channel, and K is the number of inlet channels ($K = 4$ in our systems). As a result Re_c is 4 times the ratio between D_c and D. Therefore Re_j equal to 53 and 240 correspond to Re_c of 991 and 5140, respectively.

The computational grid, which was built with design modeler and mesh, has 1,389,992 hexahedral cells: this was checked to lead to the grid independency of the obtained results. The grid comprised the whole micro-mixer, and no geometrical symmetries were used to reduce to size of the grid, in order to catch the instabilities and non-symmetrical profiles arisen from μPIV. In particular the LES model was aimed at this purpose, due to the unsteady solution it provides.

The laminar model was adopted for $Re_j = 53$; whereas, RANS standard k–ε turbulence model coupled with enhanced-wall treatment (the maximum value of y+ was 3.93), and LES model using the Smagorinsky–Lilly sub-grid model, were employed to model the flow field at $Re_j = 240$. Only for LES simulations, the time step was 0.001 s. These evaluations allowed to check the accuracy of both models in describing the velocity profiles experimentally measured by the μPIV. A second-order upwind scheme was employed for the momentum discretization in the RANS standard k–ε turbulence model, while the Bounded Central Differencing was adopted in the LES simulations. The pressure–velocity coupling was solved with the SIMPLE algorithm.

After having established the most suitable models to describe the flow field at $Re_j = 53$ and $Re_j = 240$ obtained from the μPIV, the velocity profiles of the MIVM used for MoS_2 synthesis were computed: the selected flow rates are equal to 2, 10 and 20 ml/min in each of the four inlet channels ($D = 1$ mm), corresponding to "jet" Reynolds numbers in the inlet channels Re_j of 52, 260 and 520, respectively (assuming that the aqueous solutions are both characterized by the density and viscosity of water at ambient conditions). This leads to a Reynolds number in the chamber Re_c of 832, 4160 and 8320, respectively ($D_c = 4$ mm in this case). It can be seen that the conditions at which the validation of the model against μPIV are fully representative of the ones adopted in this work for MoS_2 synthesis, although some differences in the geometry of the two MIVM still occur.

The computational grid of the MIVM for MoS_2 synthesis, which accounts for only half of the total volume for symmetrical properties of the geometry, has tetrahedral 1,187,580 cells, which was checked to lead to the grid independency. In this case, since only laminar and RANS models were adopted, the symmetry of the geometry is also accompanied by a symmetry of the flow. The laminar model was adopted for $Re_j = 52$ (2 ml/min), while the RANS standard k–ε turbulence model, coupled with enhanced-wall treatment (the maximum value of y+ was 2.63), was employed to model the flow field at $Re_j = 260$ and 520, corresponding to the conditions at 10 and 20 ml/min, respectively. A second-order upwind scheme was employed for spatial discretization, and pressure–velocity coupling was solved with the SIMPLE algorithm.

The following boundary conditions of the flow were adopted: flat profile of V_i at the channel inlets, and equal to 0.048 m/s, 0.241 m/s and 0.482 m/s for 2, 10 and 20 ml/min, respectively; discharge pressure at ambient conditions.

For the micro-mixing model, the inlets carrying one of the two solutions (for example the one which has the molybdenum(IV) complex with citric acid as key component) are characterized by $p_1 = 1$, $\xi_1 = 1$ and $\xi_2 = 0$, while in the other two inlets (characterized by the ammonium sulfide as key component, and thus by the absence of the solution carrying the molybdenum(IV) complex), the boundary conditions are $p_1 = 0$, $\xi_1 = 0$ and $\xi_2 = 0$.

The micro-mixing model equations for scalar quantities transport were solved after independently computing the internal flow field of the mixer, thus decoupling the computational effort of the two operations.

All simulations were performed with the CFD commercial code FLUENT 13, with DQMOM–IEM implemented with user-defined subroutines and scalars [23].

4. Results and discussion

As above-mentioned, the first step of this study was the computation of internal flow-field of a reference micro-mixer (Fig. 3), whose velocity profiles were measured by means of μPIV. The selection of the most suitable model (either laminar or turbulent) was based on the agreement between the velocity profiles recorded by the μPIV, and the computed ones.

The experimental measurements of the velocity profiles in the micro-mixer were available in terms of radial and tangential velocity. In particular, these two components of the velocity vector were reported for three segments lying on horizontal planes, the first one being at 1/4th of the reacting chamber height, the second one at one half, and last one at 3/4th.

As far as the experimental point at $Re_j = 53$ is concerned, a laminar model was found to provide a satisfactory agreement of the simulated and experimental points, perfectly agreeing with the profiles and conclusions enunciated in [20]: the radial and tangential velocity profiles computed with our grid and the ones measured through μPIV, are depicted in Fig. 4. Although the magnitude of the velocity is very low, which makes the accuracy of the experimental measurements difficult, the laminar model

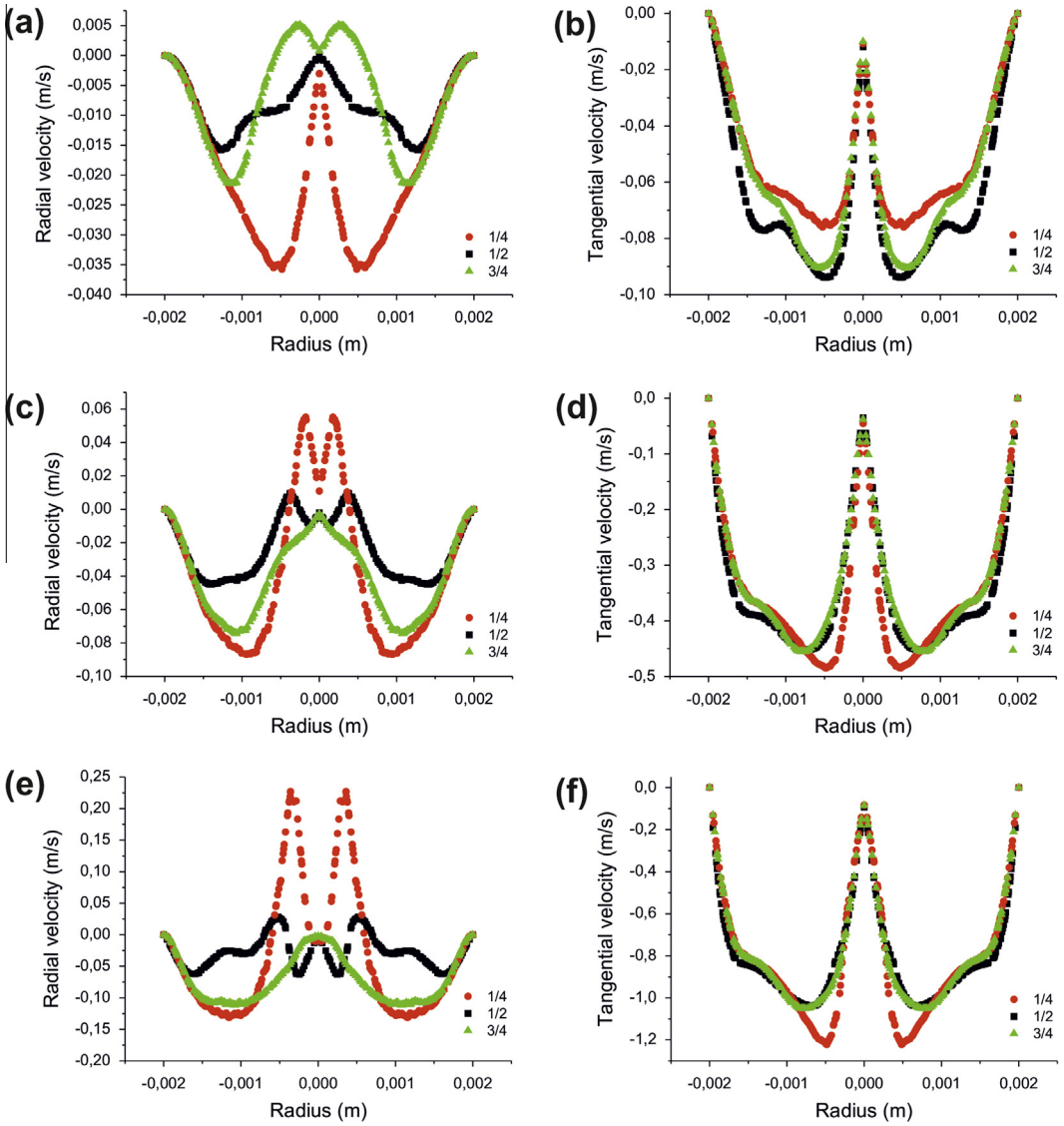

Fig. 7. Radial and tangential velocity profiles of the MIVM in Fig. 6, computed on a radial segment lying on horizontal planes at 1/4, 1/2 and 3/4 of the mixing chamber height, for Re_j of 52 (a and b), 260 (c and d) and 520 (e and f).

was able to fully catch the patterns of the flow at each investigated plane height, with minor deviations.

On the other hand, the experimental point at $Re_j = 240$ was found to require a turbulent model to be described. In fact, a laminar model strongly smoothes the swirling patter of the flow, and underestimates the magnitude of the tangential velocities. Conversely, turbulent models are more suited to this operating condition: the radial and tangential velocity profiles computed with our grid through RANS and LES models were therefore compared to the ones measured through μPIV, and the results of these simulations are depicted in Fig. 5. This result is again in agreement with the conclusions of [20], who demonstrated that even at $Re_j = 93$ (corresponding to $Re_c \sim 1600$ in our system) some unsteady motions of the fluid in the vortex core result from flow instabilities, and therefore turbulent flow occurs. This conclusion is very relevant, because it allows to apply a turbulent model in the description of the MIVM used for MoS_2 for all conditions investigated above $Re_c \sim 1600$.

It can be seen that LES is more accurate in predicting the non-uniformity of the radial profiles in transient conditions, which leads to non-symmetrical flow patterns (see μPIV experimental points at 1/4th in Fig. 5a), although both the geometry and the boundary conditions are indeed symmetrical. This acknowledges the fact that turbulent instabilities occur, and the flow is no longer laminar. RANS standard k–ε turbulence model was less accurate than LES in radial velocities computation at 1/4th and 1/2nd (Fig. 5a and c), but equally accurate at 3/4th (Fig. 5e). Concerning the tangential velocities, LES tend to overestimate the experimental value, while RANS to underestimate it, especially in the core of the mixing chamber. Given these results, the performance of the RANS model was considered as satisfactory in replicating the internal flow field of the micro-mixer; furthermore, RANS models has clear advantages in terms of computational effort with respect to LES, which makes it the most suitable choice for this kind of study. This is particularly important for the future steps of our work that will involve the simulation of the entire precipitation process. Since the precipitation kinetics for this specific systems are not known, the different unknown parameters will have to be identified; this identification would not be possible with a LES model whereas it definitely affordable with a RANS model.

After having validated the employed models for the computation of the internal flow filed of the micro-mixer described in

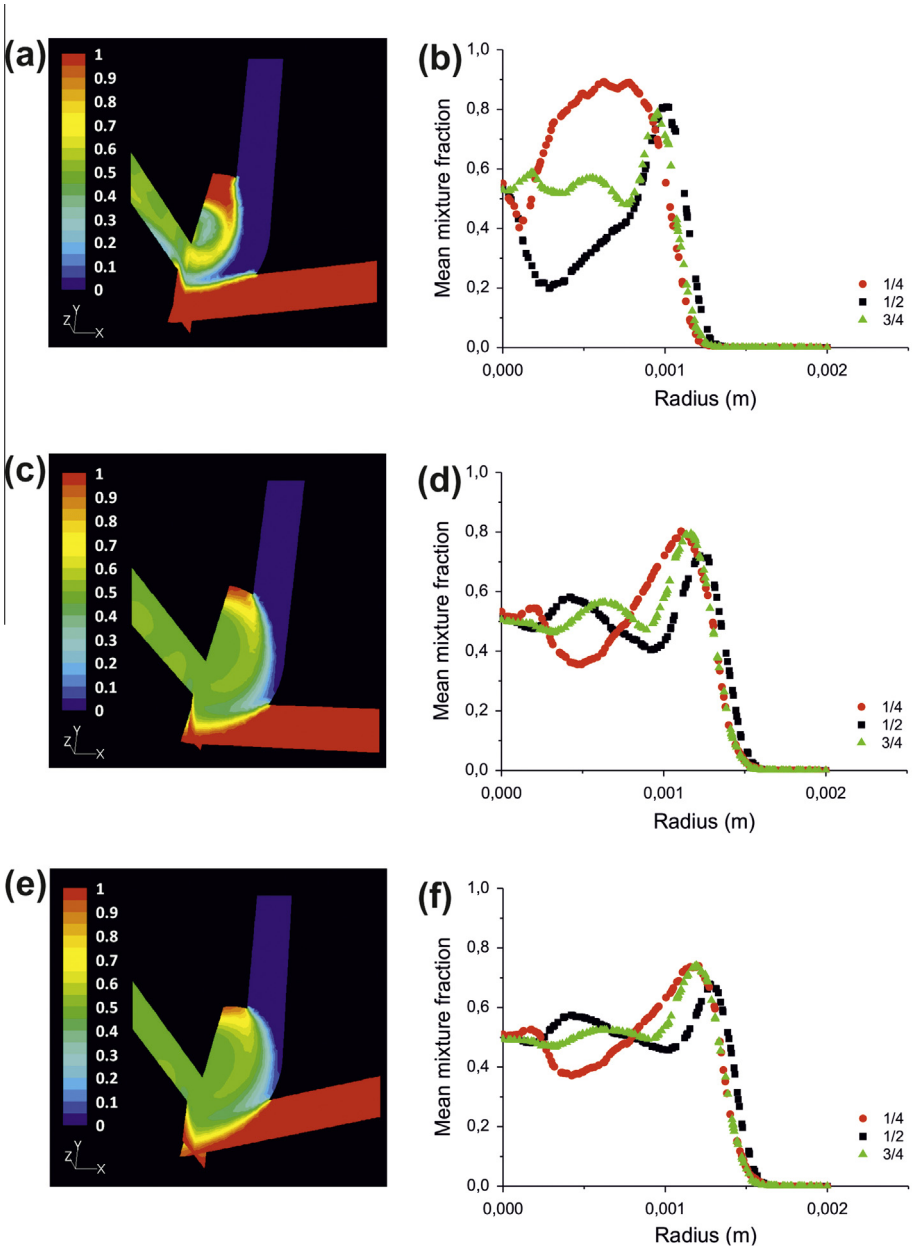

Fig. 8. Mean mixture fraction $\langle\xi\rangle$, depicted on the plane at 1/2 of the mixing chamber height (a,c,e) and computed on a radial segment lying on horizontal planes at 1/4, 1/2 and 3/4 heights (b,d and f), for Re_j of 52 (a and b), 260 (c and d) and 520 (e and f).

[20], the applications of these models was implemented in our system, to evaluate the micro-mixing occurring in the MIVM during MoS_2 production.

The MIVM profiles of radial and tangential velocity are here reported for each of the inlet flow rates investigated in this work for the synthesis of MoS_2. The same computation of the velocity profiles was adopted in this case, i.e. the components of the velocity vector were reported for three segments at 1/4th, 1/2nd and 3/4th of the mixing chamber height (Fig. 6).

For the flow rate of 2 ml/min, corresponding to a Re_j of 52, a laminar model was employed. The profiles of radial velocity appear quite different from one another, thus resulting in a less intense homogenization of the flow patterns (Fig. 7a). The velocity at the 1/4 and 1/2 planes always assume negative values, which means that the velocity is directed towards the center of the mixer while, the radial velocity at 3/4 is slightly positive towards the outlet duct (0.005 m/s), in any case indicating a simple flow pattern from the inlet to the outlet of the MIVM. The tangential velocities express the swirling flow which is established in such vortex micro-mixer (Fig. 7b).

At 10 ml/min, corresponding to a Re_j of 260, turbulent instabilities are relevant to the computation of the flow, as suggested by a Re_c of 4160. It clearly appears that, in contrast to what happens for 2 ml/min, the fluid at 1/4 is sucked in the outlet channel resulting in positive radial velocities, and tends to diverge against its walls, until a properly developed flow is established inside the duct (Fig. 7c). The tangential velocities tend now to overlap, as a result of turbulent fluctuations (resulting in large turbulent viscosity values) which produce stronger interactions between the fluid elements (Fig. 7d).

Finally, the profiles at 20 ml/min show a behavior which follows the ones already described for 10 ml/min, but with more negative values of the radial velocity at 1/4 (Fig. 7e), as well as accelerating tangential velocities at 1/4 (Fig. 7f).

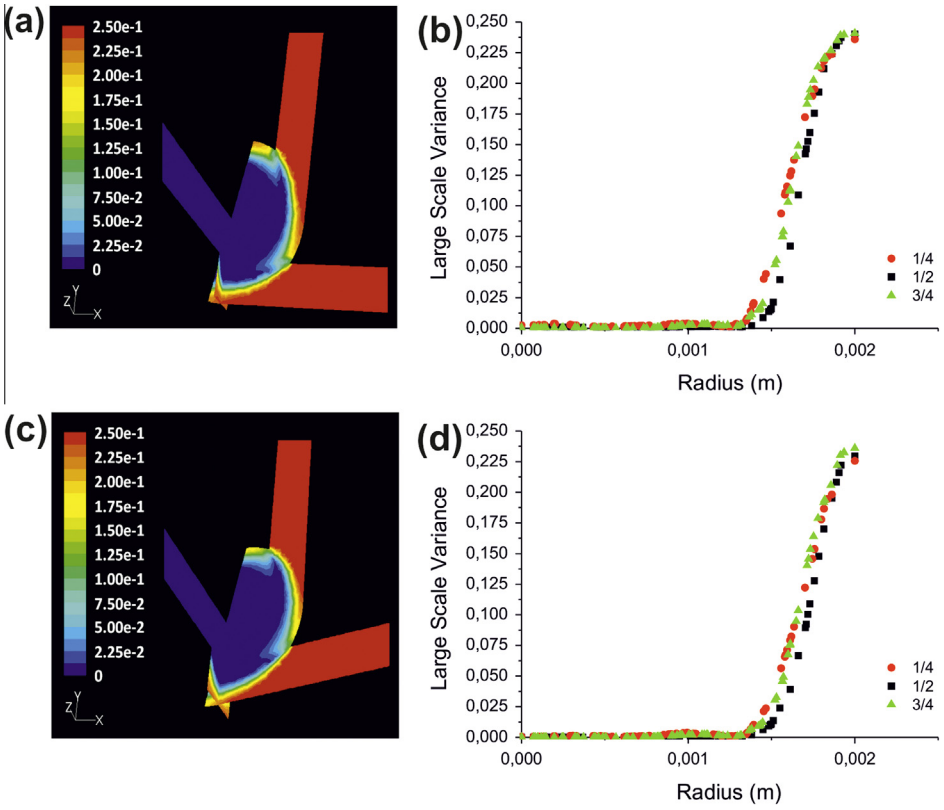

Fig. 9. Large scale variance $\langle \xi'^2 \rangle_{LS}$ of the mixture fraction, depicted on the plane at 1/2 of the mixing chamber height (a and c) and computed on a radial segment lying on horizontal planes at 1/4, 1/2 and 3/4 heights (b and d), for Re_j of 260 (a–b) and 520 (c–d).

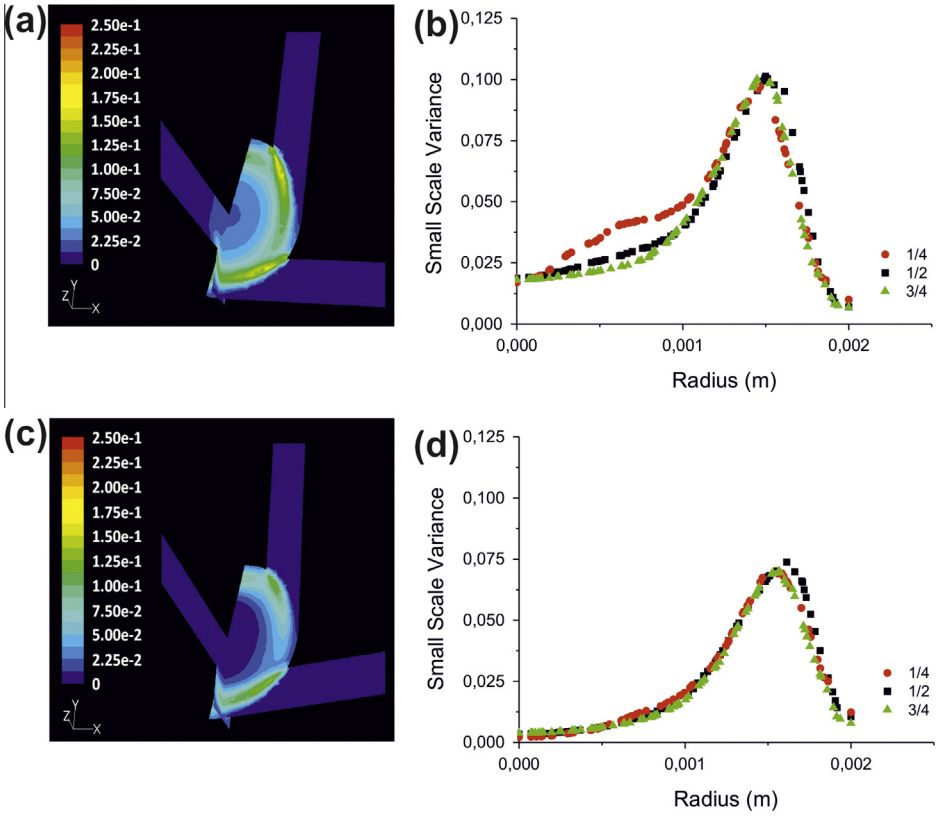

Fig. 10. Small scale variance $\langle \xi'^2 \rangle_{SS}$ of the mixture fraction, depicted on the plane at 1/2 of the mixing chamber height (a and c) and computed on a radial segment lying on horizontal planes at 1/4, 1/2 and 3/4 heights (b and d), for Re_j of 260 (a and b) and 520 (c and d).

Fig. 8 depicts the values assumed by the mean mixture fraction $\langle\xi\rangle$ in the 1/2 horizontal plane and in the vertical section of the outlet channel (Fig. 8a,c and e), along with its profile with respect to the radial coordinate computed on segments belonging to the 1/4, 1/2 and 3/4 planes (Fig. 8b,d and f). $\langle\xi\rangle$ is always comprised between 0 and 1 assuming in this particular case a value of 0.5 when mixing at the macro-scale has been completed, resulting in complete homogenization of the reactant solutions. From Fig. 8a, it can be inferred that the homogenization of the reactant concentrations is poor inside the mixing chamber, while it considerably increases under turbulent conditions (Fig. 8c and e). More precisely, one can see that $\langle\xi\rangle$ assumes very different values in the three planes at $Re_j = 52$; in particular, at 1/4 and 1/2, it approaches the value of 0.5 only close to the symmetry axis of the mixer (Fig. 8b), meaning that under these conditions mixing is very slow and nanoparticles precipitation occurs in a very inhomogeneous environment. Conversely, at Re_j of 260 and 520, $\langle\xi\rangle$ approaches 0.5 already inside the mixing chamber, which reflects the above-given considerations on the radial and tangential velocity profiles (Fig. 8d and f).

As already mentioned, macro-mixing can be assessed in terms of the large scale variance, $\langle\xi'^2\rangle_{LS}$, reported in Fig. 9: for high Reynolds numbers, $\langle\xi'^2\rangle_{LS}$ vanishes well before the exit and almost no difference can be observed between Re_j of 260 and 520 (Fig. 9a and c), and from the almost identical patterns of $\langle\xi'^2\rangle_{LS}$ at different heights of the mixing chamber (Fig. 9b and d).

However, since chemical reactions occurs between molecules the inlet fluids in the MIVM cannot be considered completely mixed if also the small scale variance, $\langle\xi'^2\rangle_{SS}$, is null. Hence, this variable quantifies the degree of mixing at the micro- (or molecular) scale and is reported in Fig. 10. Since this quantity represents the variance of the mixture fraction PDF that can be defined only for turbulent systems, results are presented here only for the higher Reynolds numbers investigated, when the flow was turbulent. Fig. 10 highlights that mixing is a cascade process: by introducing the reactants in separate inlet streams the large-scale variance is generated; subsequently, turbulent diffusion destroys the variance at this scale and generates in turn small-scale variance. This can be well appreciated from the comparison of Fig. 10b and d and Fig. 9b and d. When the $\langle\xi'^2\rangle_{LS}$ vanishes, then $\langle\xi'^2\rangle_{SS}$ peaks, as can be seen at a radial coordinate of around 0.0015 mm.

Finally, small-scale variance is eventually dissipated by molecular diffusion. For Re_j of 260 and 520, the two different turbulent intensities indeed differentiate the patterns of $\langle\xi'^2\rangle_{SS}$. In fact, at Re_j of 260 is $\langle\xi'^2\rangle_{SS}$ is about 0.03 at the planar boundary between the mixing chamber and the outlet channel, while this value is reduced to 0.008 at Re_j of 520 (Fig. 10b and d). This indicates although at both Re_j of 260 and 520 the fluids in the MIVM are fully macro-mixed only for the highest Reynolds number investigated (i.e. flow rates greater than 20 ml/min) micro-mixing is complete when the mixing chamber is left.

These results are consistent with what reported in Table 1. In fact, although no significant differences are detected in the macro-mixing dynamics between 10 and 20 ml/min measurable differences both in the average primary particle size and in the spread of the distribution were detected. These differences can be explained only in terms of the different micro-mixing behaviors observed between 10 and 20 ml/min, suggesting that at these operating conditions the precipitation process occurs at a time-scale comparable to that of turbulent fluctuations in composition, quantified by the small-scale variance.

5. Conclusions

In the present paper, the fluid-dynamics of the internal flow in a Vortex-shaped micro-mixer are investigated. In fact, this device allows tuning the degree of mixing of the chemical reactants by modifying the inlet flow rates in the reactor, in order to control the final particle size of the precipitated product. Therefore, the mixing efficacy has to be carefully assessed.

Initially, the MIVM internal flow field was investigated in order to select the proper model for viscosity estimation, i.e. laminar and turbulent models. For this case, a reference MIVM was simulated, and the obtained results were validated against μPIV [20]. Laminar conditions were the most suitable ones at low Reynolds numbers ($Re_j = 53$), while for Reynolds above $Re_j = 240$ a turbulent model should be adopted. RANS standard k–ε was found to provide satisfactory results, with a much lower computational effort than with LES. Given the strong closeness between the mixer geometry and operating conditions between the reference MIVM [20], and the one used in our work for MoS_2 synthesis, these conclusions were extended to our modeling activity.

The internal-flow field of the Vortex micro-mixer was simulated at the same operating conditions investigated in former experimental activity of MoS_2 production. Inlet flow rates of 2 ml/min, 10 ml/min and 20 ml/min, in each of the four mixer inlets, were adopted. This corresponds to laminar flow in the mixing chamber for 2 ml/min, while turbulent instabilities are established for 10 and 20 ml/min. The radial and tangential velocities of the swirling flow in the Vortex micro-mixer were computed: at 2 ml/min, the flow patterns are quite simple, and the flow is straightly directed towards the center of the mixing chamber, as can be expected in laminar flows. Conversely, in the turbulent regime, the radial velocity diverts in some points from the direction towards the center of the mixer, as evidenced by its positive value in correspondence of the outlet channel. The tangential velocities express the swirling intensity in the mixer and, at increasing turbulence, tend to overlap due to the higher effect of viscosity.

The viscous regime has implications on the degree of mixing of the two inlet solutions, and this has been computed in terms of mixture fraction of the reactants at the macro- and micro-scale, the latter through the DQMOM–IEM micro-mixing model. The mean mixture fraction profiles denote that a very poor mixing occurs at the macro-scale for the laminar flow at 2 ml/min: $\langle\xi\rangle$ is highly inhomogeneous in the volume of the mixing chamber, and hardly reach 0.5, which represents the condition of no macro-scale segregation of the reactants. Whereas, at 10 ml/min and 20 ml/min, the macro-mixing is very effective, as denoted by the flat profile of mean mixture fraction close to the mixing chamber exit in both conditions.

Finally, the micro-mixing was assessed to investigate the molecular level mixing, which is the real key factor to establish high levels of super-saturation, and thus promote nucleation. The turbulence intensity differentiates the outcome of the condition at 10 ml/min to the one at 20 ml/min, the latter providing consistently lower segregation at micro-scale.

The coupling of such turbulence and micro-mixing model with a MoS_2 nanoparticle precipitation model, including the rates of nucleation (which depend on local super-saturation of the reactants), growth (which determine the size of the primary nanoparticles at the reactor outlet) and aggregation (which depends on particle collision frequency, based on their concentrations) will be the object of next-future research investigation.

Acknowledgments

The ADDNANO project, partially funded by the European Commission as part of the 7th Framework Program, is gratefully acknowledged for the financial support. The authors also thank Eng. Simone Ripandelli and Dr. Danilo Eduardo Carvajal Araneda for their precious contribution.

References

[1] L. Rapoport, Y. Feldman, M. Homyonfer, H. Cohen, J. Sloan, J.L. Hutchison, R. Tenne, Inorganic fullerene-like material as additives to lubricants: structure–function relationship, Wear 225–229 (2) (1999) 975–982.

[2] L. Rapoport, V. Leshchinsky, I. Lapsker, Y. Volovik, O. Nepomnyashchy, M. Lvovsky, R. Popovitz-Biro, Y. Feldman, R. Tenne, Tribological properties of WS_2 nanoparticles under mixed lubrication, Wear 255 (7–12) (2003) 785–793.

[3] R. Tenne, L. Margulis, M. Genut, G. Hodes, Polyhedral and cylindrical structures of tungsten disulfide, Nature 360 (1992) 444–446.

[4] L. Cizaire, B. Vacher, T. Le Mogne, J.M. Martin, L. Rapoport, A. Margolin, R. Tenne, Mechanisms of ultra-low friction by hollow inorganic fullerene-like MoS_2 nanoparticles, Surf. Coat. Technol. 160 (2002) 282–287.

[5] L. Joly-Pottuz, J.M. Martin, F. Dassenoy, M. Belin, R. Montagnac, B. Reynard, Pressure-induced exfoliation of inorganic fullerene-like WS2 particles in a Hertzian contact, J. Appl. Phys. 99 (2006) 023524–023528.

[6] G.L. Yin, P.H. Huang, Z. Yu, D.N. He, Z.Z. Xia, L.L. Zhang, J.P. Tu, Spray drying process to synthesize multiple fullerene-like MoS_2 particles, Mater. Lett. 61 (2007) 1303–1306.

[7] X.L. Li, J.P. Ge, Y.D. Li, Atmospheric pressure chemical vapor deposition: an alternative route to large-scale MoS_2 and WS_2 inorganic fullerene-like nanostructures, Chem. Eur. J. 10 (23) (2004) 6163–6171.

[8] D. Duphil, S. Bastide, C. Lévy-Clément, Chemical synthesis of molybdenum disulfide nanoparticles in an organic solution, J. Mater. Chem. 12 (8) (2002) 2430–2432.

[9] I. Uzcanga, I. Bezverkhyy, P. Afanasiev, C. Scott, M. Vrinat, Sonochemical preparation of MoS_2 in aqueous solution: replication of the cavitation bubbles in an inorganic material morphology, M. Chem. Mater. 17 (2005) 3575–3577.

[10] S. Bensaid, J.C. Caroca, N. Russo, D. Fino, Detailed investigation of non-catalytic DPF regeneration, Can. J. Chem. Eng. 89 (2011) 401–407.

[11] J.C. Caroca, F. Millo, D. Vezza, T. Vlachos, A. De Filippo, S. Bensaid, N. Russo, D. Fino, Detailed investigation on soot particle size distribution during DPF regeneration, using standard and bio-diesel fuels, Ind. Eng. Chem. Res. 50 (5) (2001) 2650–2658.

[12] G. Santillo, F.A. Deorsola, S. Bensaid, N. Russo, D. Fino, MoS_2 nanoparticle precipitation in turbulent micromixers, Chem. Eng. J. 207–208 (2012) 322–328.

[13] D.H. Killeffer, Molybdenum compounds: their chemistry and technology, Interscience Publication, New York, 1952.

[14] R.K. Thakur, Ch. Vial, K.D.P. Nigam, E.B. Nauman, G. Djelveh, Static mixers in the process industries – a review, Chem. Eng. Res. Dev. 81 (2003) 787.

[15] F. Lince, D.L. Marchisio, A.A. Barresi, A comparative study for nanoparticle production with passive mixers via solvent-displacement: use of CFD models for optimization and design, Chem. Eng. Proc. 50 (2011) 356–368.

[16] J. Gradl, H.C. Schwarzer, F. Schwertfirm, M. Manhart, W. Peukert, Precipitation of nanoparticles in a *T*-mixer: coupling the particle population dynamics with hydrodynamics through direct numerical simulation, Chem. Eng. Process. 45 (2006) 908–916.

[17] Y. Liu, J.C. Cheng, R.K. Prud'homme, R.O. Fox, Mixing in a multi-inlet vortex mixer (MIVM) for flash nano-precipitation, Chem. Eng. Sci. 63 (2008) 2829–2842.

[18] B.K. Johnson, R.K. Prud'homme, Chemical processing and micromixing in confined impinging jets, AIChE J. 49 (2003) 2264–2282.

[19] Y. Liu, R.O. Fox, CFD predictions for chemical processing in a confined impinging-jets reactor, AIChE J. 52 (2006) 731–744.

[20] J. Cheng, M. Olsen, R. Fox, A microscale multi-inlet vortex nanoprecipitation reactor: turbulence measurement and simulation, Appl. Phys. Lett. 94 (2009) (204104/1–3).

[21] R.O. Fox, On the relationship between Lagrangian micromixing models and Computational Fluid Dynamics, Chem. Eng. Proc. 37 (1998) 521–535.

[22] D.L. Marchisio, R.O. Fox, Solution of population balance equations using the direct quadrature method of moments, J. Aerosol Sci. 36 (2005) 43–73.

[23] N. Di Pasquale, D.L. Marchisio, A.A. Barresi, Model validation for precipitation in solvent-displacement processes, Chem. Eng. Sci. 84 (2012) 671–683.

[24] R.O. Fox, Computational models for turbulent reacting flows, Cambridge University Press, 2003.

[25] A.E. Lewis, Review of metal sulphide precipitation, Hydrometallurgy 104 (2010) 222–234.

[26] J.C. Cheng, A comprehensive model study for flash nanoprecipitation: computational fluid dynamics, micro-particle image velocimetry, and population balance modeling, PhD Thesis, Iowa State University, 2010.